Journal of
Materials Chemistry A

PAPER

View Article Online
View Journal | View Issue

Published on 15 May 2017. Downloaded by University of California - Berkeley on 7/20/2018 5:36:13 PM.

Cite this: J. Mater. Chem. A, 2017, 5, 11905

Phosphate tuned copper electrodeposition and promoted formic acid selectivity for carbon dioxide reduction†

Jian Zhao,[abcd] Libo Sun,[ac] Silvia Canepa,[e] Hongyu Sun,[e] Murat Nulati Yesibolati,[e] Matthew Sherburne,[df] Rong Xu,[dg] Thirumany Sritharan,[ad] Joachim S. C. Loo,[ac] Joel W. Ager III,[df] James Barber,[ch] Kristian Mølhave[e] and Zhichuan J. Xu*[abcd]

Fabrication of catalytically active electrodes by electrodeposition is attractive due to its *in situ* nature, easy controllability, and large-scale operation capability. Most recently, modifying the electrodes with phosphate ligands through electrodepositing electrode materials has shown promising results in improving the kinetics of some reactions. However, it is unclear how the presence of phosphate anions affects the electrodeposition process and functions in catalyzing reactions. Here, we report a systematic study on electrodeposition of Cu in the presence of phosphate anions. The phosphate anions form a complex with free Cu(II) cations, competing with the electrodeposition process. The competition between the two processes results in an insufficient supply of free Cu(II) for electrodeposition, especially at the diffusion layer. This is evidenced by the calculation of free Cu(II) concentration and the electrodeposition current at identical applied potentials. We also found that the electrodeposition of Cu in the presence of phosphate generates Cu-oxyo/hydroxyo-phosphate species on the deposited copper surface. The modified electrodes with phosphate species exhibit higher selectivity for HCOOH formation (faradaic efficiency ~80%) from the electrochemical reduction of CO_2 as compared with Cu foil (faradaic efficiency ~33%). The effect of phosphate ligands promoting HCOOH selectivity is further verified by stripping off the ligands and regenerating the ligands.

Received 1st March 2017
Accepted 15th May 2017

DOI: 10.1039/c7ta01871a

rsc.li/materials-a

Introduction

Copper is an earth-abundant element and has been used in catalysis for a long time. For example, heterogeneous copper catalysts are well known for use in hydrogenation and oxidation of small molecules.[1–4] Recently, the intense research interest in CO_2 electrochemical reduction has led to a focus of attention on metallic Cu electrodes due to their unique ability for hydrocarbon production.[5–10] It has been found that the surface properties of the Cu electrode influence the product selectivity[11–15] as well as the overpotential.[11] Much effort has been made on modifying the surface of bulk Cu thin film electrodes, including film preparation,[16] surface treatment,[11,17] ligand modification,[18,19] alloying,[20] *etc.* The preparation methods directly determine the surface properties of Cu thin film electrodes, such as roughness, crystal orientation, and chemical composition, which further determine their catalytic activity and the strategies required for surface modification. The preparation methods reported for bulk Cu thin film electrodes include electrodeposition,[21–25] polishing Cu foil,[5] sputter coating,[26] pulsed laser deposition (PLD),[27] *etc.* Of these methods, electrodeposition is preferred due to its low cost and simple operation. Most importantly, the deposition is made on conductive substrates and the surface crystal properties of electrodeposited electrodes can be controlled by varying the overpotential and deposition electrolyte.

During electrodeposition, the surface free energy mainly governs the crystal shape under or near the thermodynamic equilibrium conditions. When the system is driven far from equilibrium (high overpotential), mass transport, and surface properties play a dominant role in determining the shape of

[a]School of Materials Science and Engineering, Nanyang Technological University, Singapore. E-mail: xuzc@ntu.edu.sg
[b]Energy Research Institute @ Nanyang Technological University, Singapore
[c]Solar Fuels Laboratory, Nanyang Technological University, Singapore
[d]Singapore-Berkeley Research Initiative for Sustainable Energy, 1 Create Way, Singapore
[e]Department of Micro- and Nanotechnology, Technical University of Denmark, 2800 Kongens, Lyngby, Denmark
[f]Materials Science and Engineering, University of California, Berkeley, USA
[g]School of Chemical and Biological Engineering, Nanyang Technological University, Singapore
[h]Department of Life Sciences, Imperial College London, London, UK

† Electronic supplementary information (ESI) available: HPLC and GC calibration, SEM images and XRD pattern of deposited Cu on FTO, product analysis, calculation for the reference electrode, *etc.* can be found. See DOI: 10.1039/c7ta01871a

Published on 15 May 2017. Downloaded by University of California - Berkeley on 7/20/2018 5:36:13 PM.

deposited crystals.[28–32] Strategies that have been reported for surface morphology control during electrodeposition include tuning the overpotential, adjusting the precursor concentration, adding additives,[25,29,30,32–36] *etc.* For example, by increasing the overpotential, metal ions can be consumed faster than their transport rate. The crystal growth is then limited by the diffusion of free metal ions instead of their reduction rate. Due to the insufficient supply of free metal ions, the reductive deposition of metal becomes location-selective. The deposition preferentially occurs at the corners of crystals to form branched-3D-structures. An explanation for this phenomenon is that the electric fields converge at the corners, creating higher current densities of electromigration in the depletion layer at protrusions than that at the flat parts, which drives the deposition preferentially at the corners.[37] In contrast, adding additives controls the morphology of the deposited crystals mainly through preferential adsorption on certain facets thereby inhibiting the growth of these facets.[25]

In our previous work, we investigated the electro-reduction of Cu_2O films in the presence of phosphate additives.[38] It was found that the phosphate anions adsorbed onto the electrode surface and promoted the local proton concentration. Since this is not a deposition process, the shape variation induced by additive preferential adsorption was not observed. However, it indicates a strong interaction between phosphate ligands and Cu ions.

The strong interaction between phosphate and Cu ions is well known.[39–41] Phosphate anions interact with Cu(II) forming complexes in aqueous solution.[42–44] The thermodynamically possible complexes are $Cu(HPO_4)^0$, $Cu(H_2PO_4)^+$, sparingly soluble precipitates $[Cu_3(PO_4)_2]$, and multiple hydrolyzed forms like libethenite $[Cu_2(PO_4)(OH)]$, cornetite $[Cu_3(PO_4)(OH)_3]$, reichenbachite $[Cu_5(PO_4)_2(OH)_4]$, and pseudomalachite $[Cu_5(PO_4)_2(OH)_4 \cdot H_2O]$.[42–46] The formation of complexes leads to a decrease in free Cu(II) ions in the solution. If Cu electrodeposition is done in the presence of phosphate anions, one could hypothesize that a chemical equilibrium will be attained between the free Cu(II) ions and formed complexes. Subsequently, on driving the electrodeposition, a competition is created for free Cu(II) ions between the processes of complex formation and electrodeposition. As a result, mass transport-limited deposition could be achieved with a lower overpotential.

This article presents our recent study to verify the above hypothesis. It includes a systematic study on the electrodeposition of Cu thin films on Cu foil and FTO in the presence of phosphate ions, as well as the product selectivity of the as-deposited Cu films for CO_2 electrochemical reduction. By adjusting the applied potential and the phosphate concentration, the morphology of the deposited Cu was varied from particles, to hexagonal-plates, and then to branched-3D-structures. Direct evidence for phosphate-mediated, mass transport-limited deposition is given by recording the limiting deposition currents at various concentrations of phosphate. The deposited Cu electrodes exhibited much higher formic acid selectivity than Cu foil electrodes for CO_2 electrochemical reduction in acetonitrile. Furthermore, the experiments indicate that the adsorbed phosphate ligands play an important role in promoting HCOOH production.

Experimental

Chemicals

Copper foil (99.99%), potassium phosphate monobasic (Sigma-Aldrich, 99%), acetonitrile anhydrous (Sigma-Aldrich, 99.8%), tetrabutylammonium tetrafluoroborate (Aldrich, 99%), and copper(II) sulfate pentahydrate (Sigma-Aldrich, 98.0%).

Electrodeposition

A three-electrode cell system was used to electro-deposit copper. 1×1 cm^2 Cu foil slides and F-doped SnO_2 (FTO) glass were used as working electrodes. FTO was pre-treated *via* sonication in deionized water, acetone, and ethanol for 20 min. Cu foil slides were treated by electro-polishing in 85% *o*-phosphoric acid at 4 V *versus* a graphite counter electrode for 1 min and then washed with deionized water. Before use, both substrates were dried using nitrogen gas. A coiled platinum wire was used as the counter electrode. The distance between the working and the counter electrodes was 0.5 cm. Ag/AgCl with 1 M KCl was used as the reference electrode. All electrodeposition experiments were performed at room temperature without stirring. The deposition solution contained 0.02 M $CuSO_4$. The concentration of phosphate (KH_2PO_4) was varied from 0 to 25 mM in the deposition solution. The deposition potential was varied and the morphology evolution of deposited crystals was investigated. The deposition time was 600 s if not otherwise specified.

Characterization

The morphologies of the deposited Cu films were investigated by using a JEOL 7600F field emission scanning electron microscope (FE-SEM) operating at 5 kV. Energy dispersive X-ray spectroscopy (EDS-mapping) was conducted using the same scanning electron microscopy (SEM) instrument at an operating voltage of 15 kV. X-ray diffraction (XRD) patterns were recorded using a Shimadzu XRD-6000 X-ray diffractometer (Cu Kα source) with the 2θ range from 28 to 78° at a scan rate of 4° min^{-1}. Attenuated total reflectance–Fourier transform infrared spectroscopy (ATR-FTIR) was performed using a PerkinELmer FT-IR/NIR spectrometer frontier with a universal ATR sampling accessory. Zeta potential was measured by using an HORIBA Scientific nanoparticle analyzer instrument with carbon electrode cells (6 mm). The *in situ* TEM was conducted in a custom made electrochemical TEM liquid cell holder with an FEI Tecnai TEM operating at 200 kV and an electron dose rate of 116 e$^-$ nm^{-2} s^{-1}. The electrolyte solution was encapsulated between two clamped silicon microchips, each with a 50 nm thick, 50 μm × 200 μm large electron transparent silicon nitride (SiN_x) membrane, which serves as the imaging window. In one of the chips, Au electrodes (with a width of 5 μm) were patterned on top of the nitride membrane.

Electrochemical reduction of carbon dioxide

CO_2 reduction was performed at room temperature in a gas-tight two-compartment electrochemical cell controlled with an Autolab PGSTAT-30 potentiostat. A Nafion® perfluorinated

 This journal is © The Royal Society of Chemistry 2017

Published on 15 May 2017. Downloaded by University of California - Berkeley on 7/20/2018 5:36:13 PM.

membrane was used to separate the electrolyte. Before use, the membrane was boiled in 3–5% H_2O_2 for 30 min, in deionized water for 30 min, in 0.5 M H_2SO_4 for 1 h, finally in deionized water for 1 h. The electrolyte was 0.1 M tetrabutylammonium tetrafluoroborate in acetonitrile without further drying treatment, which is also known as "wet" acetonitrile because no further drying of any of the chemicals was done. The water content is 46–528 ppm or 0.0046–0.0528%, which mainly depends on the supporting electrolyte used.[47] The influence of water content in this small range should be negligible. The electrolyte was saturated with CO_2 before the reaction. Pt wire was used as the counter electrode and non-aqueous Ag/Ag^+ (10 mM $AgNO_3$, 0.1 M tetrabutylammonium tetrafluoroborate in acetonitrile) was used as the reference electrode. The reference electrode was calibrated using the redox of Fc^+/Fc (the detailed information is provided in the ESI†). Gas products were detected and analyzed by gas chromatography with a TCD detector (Agilent 7890A) and a molecular sieve packed column with argon carrier gas. The liquid products were analyzed by high-performance liquid chromatography (Agilent 1260 HPLC with a VWD detector and Alltech OA-1000 organic acid column). Before the HPLC test, the liquid product was diluted with deionized water (15% v/v water). The detailed HPLC condition and the calibration information are provided in the ESI (Table S1 and Fig. S1†).

Results and discussion

Film characterization

Fig. 1 presents the SEM images of Cu films deposited on Cu foil substrates. From top to bottom, the applied deposition potential increases from −0.25 V to −0.6 V. From left to right, the concentration of phosphate increases from 0 mM to 25 mM. An increase in the concentration of phosphate beyond 25 mM will result in the precipitation of copper phosphate (Fig. S2†). The general trend apparent in Fig. 1 is that increasing both the variables, overpotential and phosphate concentration, will promote the development of branched-3D-structures. For example, under the potential of −0.4 V, increasing the phosphate concentration from 0 to 25 mM changed the morphology of deposited Cu from particles to hexagonal plates, and then to branched 3D structures, while at the fixed phosphate concentration of 5 mM, increasing the deposition potential from −0.25 V to −0.6 V resulted in a similar morphology evolution.

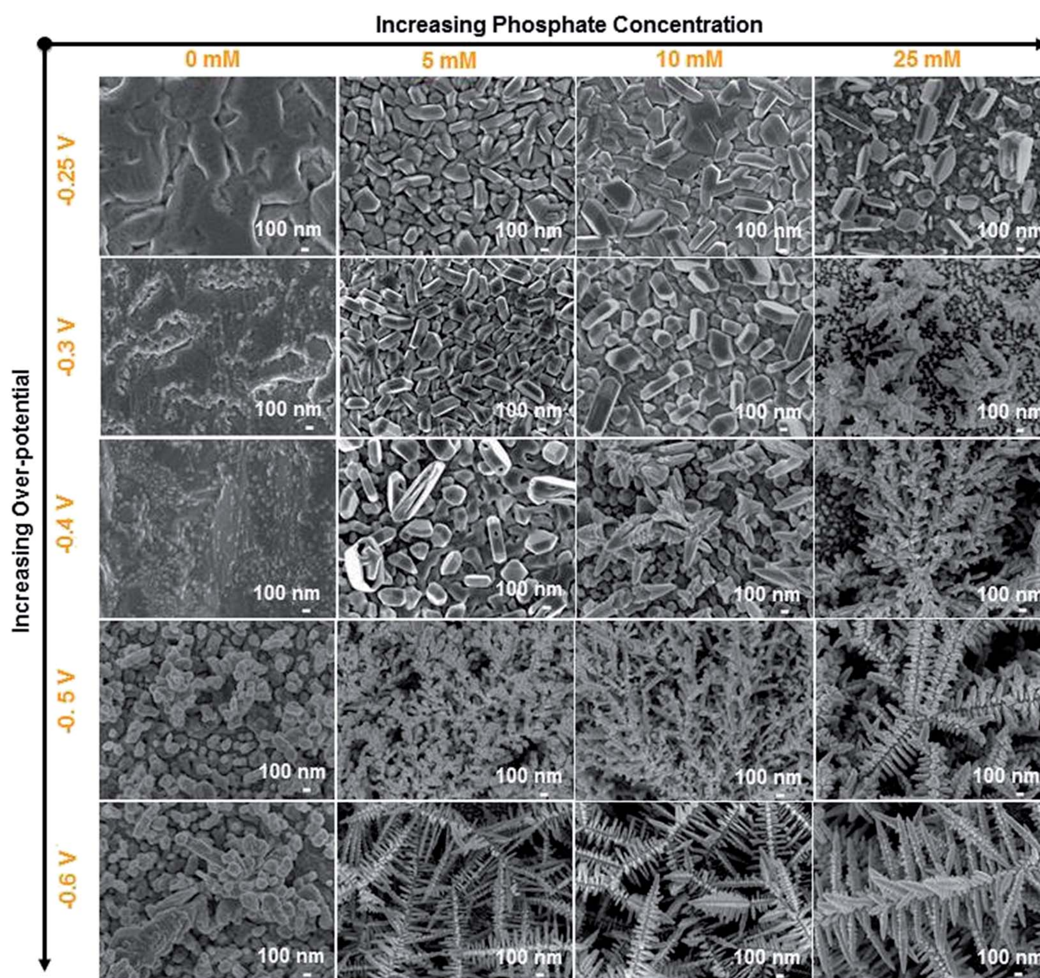

Fig. 1 The Cu crystals deposited in the absence and the presence of phosphate on Cu foil slides with 0.02 M $CuSO_4$. The potential is in V *vs.* Ag/AgCl for the electrodeposition.

Published on 15 May 2017. Downloaded by University of California - Berkeley on 7/20/2018 5:36:13 PM.

The morphology evolution towards branched 3D structures could be ascribed to the mass transport-limited growth.[32,48] At low overpotentials, the reduction rate of free Cu(II) ions is relatively slow and the depletion of Cu(II) ions near the electrode surface could be readily replenished by diffusion from the bulk solution. Under this growth condition the Cu crystals grow surrounded by sufficient Cu(II) ions so that the dominant crystal shape determining criterion is minimization of total surface energy. This situation is referred to as the reduction-controlled or overpotential-limited growth near the equilibrium conditions.[32,48] As the applied potential is further increased, free Cu(II) ions near the electrode will be consumed faster than their diffusion rate. Then the factor other than surface energy, mass transport, plays the dominant role here in determining the crystal shapes. The crystal growth becomes limited by the supply of free Cu(II) ions (mass transport-limited growth). Under this condition, thermodynamically unstable branched-3D-structures are formed as evident in Fig. 1. As more phosphate is added to the deposition solution, branched-3D-structures become increasingly possible at lower overpotentials.

This implies that the presence of phosphate reduces the available Cu(II) ions for feeding the crystal growth, which makes the deposition process mass-transport-limited even at a low reduction rate. To eliminate the possibility that the adsorption of phosphate ions on certain facets might have induced the formation of 3D structures, we did control experiments with a higher overpotential and a lower Cu(II) precursor concentration, but without phosphate addition. A similar branched-3D-structure was obtained at −0.8 V (Fig. S3a†). With a lower $CuSO_4$ concentration of 0.01 M, a similar morphology was also achieved at −0.6 V (Fig. S3b†).

In Fig. 2, we have performed *in situ* TEM experiments to follow the growth of Cu dendrites in real time. The deposition was done on 50 nm gold electrodes from a 20 mM $CuSO_4$ solution with and without addition of 25 mM phosphate. The system uses other nearby gold electrodes as the counter- and pseudo-reference electrodes, so the potentials are not directly comparable to those in experiments done *ex situ* with a suitable reference electrode, but will indicate similar trends. The TEM study clearly shows the smoother growth at lower voltages and in solutions without phosphate, while dendrites are formed with phosphate solutions and higher potentials.

Fig. 3 shows the XRD patterns of deposited Cu crystals. It can be seen that the deposited Cu is crystalline and purely in the metallic (fcc) Cu phase. The Cu foil substrate has a (200) texture as evident in Fig. 3a. The preference for the deposited Cu crystals changes when the potential and phosphate concentration are changed. Fig. 2b–d show the XRD patterns of Cu crystals deposited at −0.25, −0.4, and −0.6 V in the absence of phosphate. It can be seen that (220) is their preferred orientation at low overpotentials (*e.g.* at −0.25 V and −0.4 V). With increasing overpotential, the intensity ratio of (111)/(220) peaks increased from 0 to 1.16, indicating that the preferred orientation changes to (111). This is consistent with the other reports that indicate that (111) is usually the most common texture in Cu films.[25,37] This dependence of orientation preference on potential exists in the Cu crystals deposited in the presence of phosphate also. For example, Fig. 3e–g show the XRD patterns

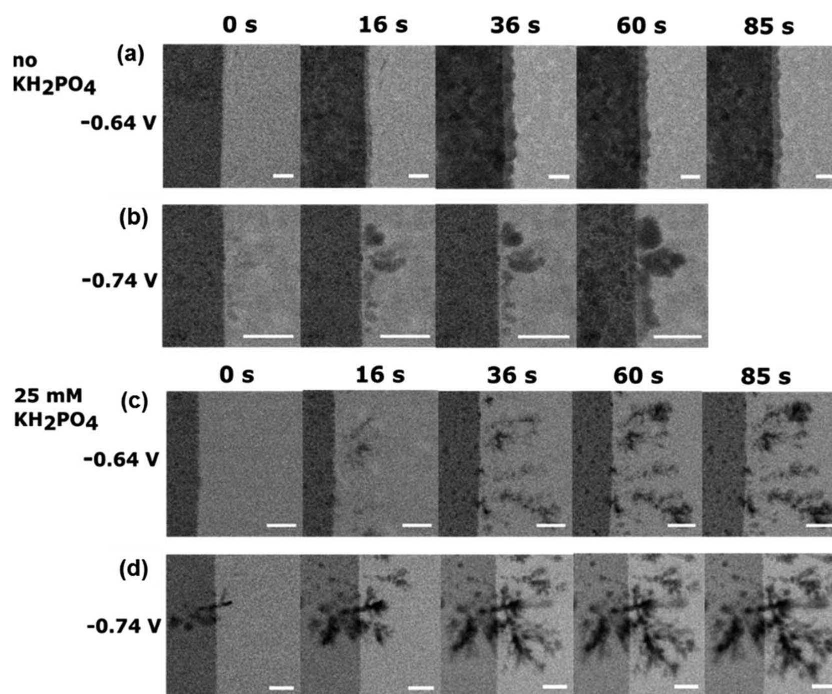

Fig. 2 (a–b) Time-lapse images showing Cu electroplating on the Au electrode from an aqueous solution of 20 mM $CuSO_4$ with an applied overpotential relative to a pseudo-reference electrode of −0.64 V (a) and −0.74 V (b). (c–d) The same with an aqueous solution of 20 mM $CuSO_4$ + 25 mM KH_2PO_4 with an applied overpotential of −0.64 V (c) and −0.74 V (d). The beam electron dose rate is 116 e^- nm^{-2} s^{-1}. Scale bar is 500 nm.

 This journal is © The Royal Society of Chemistry 2017

Published on 15 May 2017. Downloaded by University of California - Berkeley on 7/20/2018 5:36:13 PM.

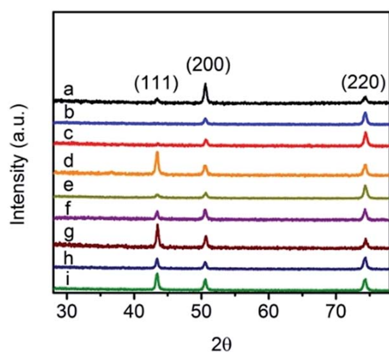

Fig. 3 XRD patterns of Cu foil (a); Cu crystals deposited in the absence of phosphate at −0.25 V (b), −0.4 V (c), and −0.6 V (d); Cu crystals deposited in 5 mM phosphate at −0.25 V (e), −0.4 V (f), and −0.6 V (g); Cu crystals deposited in 25 mM phosphate at −0.25 V (h) and −0.6 V (i).

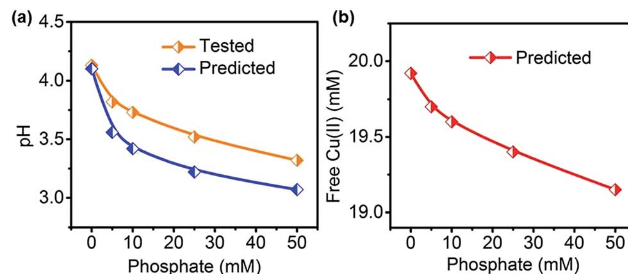

Fig. 4 (a) The pH values at different phosphate concentrations obtained by calculation and measurement. The calculation is made based on the equilibrium reactions listed in Table 1. (b) The calculated free Cu(II) concentration for the deposition solutions containing 0.02 M $CuSO_4$ as a function of phosphate concentration.

of Cu deposited with 5 mM phosphate. The intensity ratio of (111)/(220) increased from 0.88 to 1.56 as the deposition potential increases from −0.25 to −0.6 V, which implies that (111) again is preferred at high overpotentials. In the presence of 25 mM phosphate (Fig. 3h and i), the intensity ratio of (111)/(220) also increases with the increase of the overpotential. The increased intensity of (111) has been observed in other deposition studies, where the current density and deposition time were the two parameters used to control orientation.[48,49] As for the current density, it determines the deposition kinetics. At a high deposition rate, the supply of free cations becomes insufficient and thus 1D fcc crystals oriented in (111) can be produced. For the deposition time, it was found that longer deposition time also gives (111) as the preferred orientation. This is probably because the (111) planes have the lowest surface energy in fcc crystals.[49,50]

Fig. S4† shows the SEM images of Cu deposited on FTO glass slides under the same conditions. A morphology evolution somewhat similar to Cu deposited on Cu foil slides was observed. With the increase of the deposition potential, the morphology changed from particles to leaf-like branched particles. Increasing the phosphate concentration also resulted in this morphology evolution. However, a slight difference can be noticed in Fig. S4.† The Cu crystals deposited on FTO substrates did not fully cover the substrate area but formed islands resulting in low density. In contrast, the Cu crystals deposited on Cu foil substrates are closely packed together with a much high density. This is probably due to the nature of the substrates. The large crystal lattice mismatch between FTO and Cu thermodynamically suppresses the nucleation of Cu on FTO. Fig. S5† shows the XRD patterns of Cu crystals deposited on FTO substrates. All patterns show the metallic (fcc) Cu phase and in this case proportional to the powder pattern with intensity depending on the amount of Cu deposited as there is no underlying texture. Different Cu precursors (*e.g.* SO_4^{2-} and NO_3^-) had no influence on the crystal morphology. The result of using $Cu(NO_3)_2$ as the precursor was similar to the morphology obtained from $CuSO_4$.

Complexation of phosphate with Cu(II)

Our study of the morphology evolution has shown that phosphate dramatically influences the deposition process. Even at the slow reduction rates (low overpotential), branched-3D-structures could still be formed. This implies that there is an insufficient supply of free Cu(II) ions due to the complexation of Cu(II) with phosphate. Therefore, the complexation in the deposition solution was investigated in this work. Fig. 4 shows the pH variation upon the addition of phosphate. The pH value of the original deposition solution (0.02 M $CuSO_4$) without phosphate was 4.13. It is due to the formation of $Cu(H_2O)_5(OH)]^+$ and $[H–H_2O]^+$ ($pK_c = 6.5$). Introducing phosphate further decreased the pH value. The pH values for 5, 10, 25, and 50 mM phosphate are 3.82, 3.73, 3.52, and 3.32, respectively. It should be noted that adding 50 mM phosphate resulted in the precipitation of $Cu_3(PO_4)_2\cdot 3H_2O$ (Fig. S2†). The general trend of the decrease of pH with the addition of phosphate indicates the formation of a complex between Cu(II) and phosphate. Table 1 lists the equilibrium reactions involving Cu(II) and their corresponding pK_c at 25 °C. Using these equations and constants, we could calculate the pH and free Cu(II) concentration after complexation with phosphate ligands (Fig. 3). The calculated pH is basically in agreement with the measured pH (Fig. 4a). Also as shown in Fig. 4b, free Cu(II) decreases with the increase in the phosphate concentration. However, as stated in the first section, with a low $CuSO_4$ concentration (0.01 M), a similar morphology could be also achieved at −0.6 V (Fig. S3b†). Here, as calculated in Fig. 4b, the decrease of free Cu(II) is less than 1 mM with the addition of phosphate anions. There may be another possibility that the adsorption of complexes formed between phosphate and Cu(II) inhibited the free Cu(II) transport near the electrode surface. This inhibition layer may make the

Table 1 The equilibrium reactions of copper(II) ions in aqueous solution and the corresponding pK_c at 25 °C (ref. 51)

Equilibrium reactions of Cu(II)	pK_c
$Cu^{2+} + H_2PO_4^- \rightarrow CuHPO_4^0 + H^+$	3.112
$3Cu^{2+} + 2H_2PO_4^- + 3H_2O \rightarrow Cu_3(PO_4)_2\cdot 3H_2O(\downarrow) + 4H^+$	0.999
$Cu^{2+} + 7H_2O \rightarrow [Cu(H_2O)_5(OH)]^+ + [H–H_2O]^+$	6.5

Published on 15 May 2017. Downloaded by University of California - Berkeley on 7/20/2018 5:36:13 PM.

mass-transport-limited deposition more obvious, which leads to the formation of 3D structures with the addition of phosphate at a very low overpotential. A similar finding about the copper phosphate complex layers on copper surfaces has been reported during the copper pipe corrosion in water supply.[39–41] Although TEM study shows that there is no obvious formation of thick deposits in front of the growing Cu deposit, thinner layers cannot be ruled out.

The deposition *I*–*t* curves also should reflect the influence of the phosphate concentration on free Cu(II) supply. Fig. 5a shows the deposition currents at −0.4 V with different phosphate concentrations as a function of time. With the increase of the phosphate concentration, the current decreased even though the concentration of $CuSO_4$ was fixed for all cases. This is clear evidence that the supply of free Cu(II) ions at the electrode surface is affected by the addition of phosphate ions. It further supports the mechanism of mass transport-limited deposition resulting in branched-3D-structures. The same current change trend exhibited at −0.5 (Fig. 5b) and −0.6 V (Fig. 5c) also decreases with the increase of the phosphate concentration. Fig. 5d is a double logarithmic plot of the stable deposition current (log *i*) against the phosphate concentration (log C_P), which shows a linear relationship. The slopes for deposition at −0.4, −0.5, and −0.6 V are −0.12, −0.13, and −0.20, respectively. These slopes are negative, unlike in the systems where phosphate is used as a proton transfer medium for water splitting reactions.[38,52] In those systems, the catalytic currents increase with the increase in the phosphate concentration. It is attributed to the faster proton transfer kinetics on the addition of more phosphate. In our deposition system, adding more phosphate caused more Cu(II) consumption through complexation, reducing the free Cu(II) available for the deposition process. The copper phosphate complexes may also form an adsorption layer on the copper surface, further reducing the availability of free Cu(II) for the deposition process. As a result, the deposition process ($Cu^{2+} + 2e^- \rightarrow Cu$) gets suppressed, leading to a decrease in the deposition current accordingly. We also found that the slopes increased with an increase of the applied potential. This is probably because at higher deposition potentials, free Cu(II) ions were consumed faster. Thus, the complexation process is more pronounced at higher overpotentials.

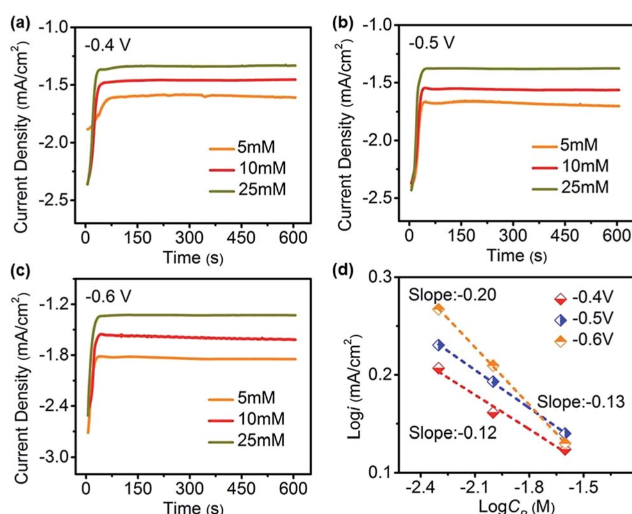

Fig. 5 (a) The recorded *I*–*t* curves for the deposition solutions (0.02 M $CuSO_4$) with 5, 10, and 25 mM phosphate at (a) −0.4 V, (b) −0.5 V, and (c) −0.6 V; (d) corresponding logarithm current (log *i*) as a function of the logarithm of phosphate concentration (log C_P).

The function of phosphate can be further demonstrated by comparing the quantity of deposited Cu at different phosphate concentrations. The quantity of deposited Cu was calculated from the moles of electrons involved in a deposition time of 600 s [$Cu^{2+} + 2e^- \rightarrow Cu$, $n(Cu) = 1/2n(e^-)$] using Faraday's Laws [$n(e^-) = Q/F$]. Q was recorded during the deposition (charges in C) and F is the Faraday constant (96 500C mol^{-1}). As shown in Fig. 6a, the quantity of deposited Cu decreased with the increase of the phosphate concentration. The logarithm of deposited Cu quantity is in a negative linear relationship with the logarithm of phosphate concentration (Fig. 6b). This is consistent with the observations from the deposition current, and again confirms the function of phosphate anions on free Cu(II) supply for electrodeposition through the complexation.

Knowing the deposition current, the concentration of free Cu(II) ions at the thickness of the diffusion layer $\delta(t) = D^{1/2}t^{1/2}$ after certain deposition time (t) can be calculated using the Cottrell equation; for the transient build-up of a depletion layer at an electrode as a function of time, the current density decays as follows: $I_t(t) = nFAC\sqrt{D/\pi t}$. At longer time lengths a steady state diffusion through the stagnant depletion layer will give a steady current $I_s(t) = nFACD/\delta$ where A is the area of the electrode (cm^{-2}), D is the diffusion coefficient of Cu(II) ($cm^2\ s^{-1}$), C is the bulk concentration of free Cu(II) ions (mol cm^{-3}), n is the number of electrons to reduce one molecular Cu(II), F is the Faraday constant (96 500C mol^{-1}), and t is the deposition time (s). The diffusion coefficient of ions varies at different concentrations but this variation is limited even when the concentration of ions changed over several orders of magnitude. For example, the diffusion coefficients of 0.02, 0.01, and 0.0001 M Cu(II) ions are $6.9 \times 10^{-6}\ cm^2\ s^{-1}$, $7.2 \times 10^{-6}\ cm^2\ s^{-1}$, and $7.7 \times 10^{-6}\ cm^2\ s^{-1}$, respectively (Table S2†).[53,54] In our deposition solutions, the concentration of $CuSO_4$ is 0.02 M. The proton concentration (pH value) is contributed by both complexation and phosphate dissociation. Assuming that all protons are generated from the complexation process

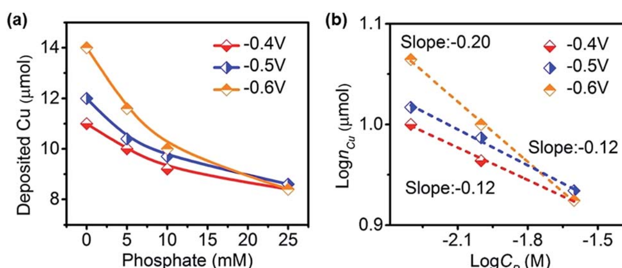

Fig. 6 (a) The quantity of deposited Cu in 600 s as a function of phosphate concentration. (b) The corresponding logarithm of the curves in (a).

 This journal is © The Royal Society of Chemistry 2017

Published on 15 May 2017. Downloaded by University of California - Berkeley on 7/20/2018 5:36:13 PM.

(including $Cu(H_2O)_5(OH)]^+$ formation), the Cu(II) ions consumed by complexation are calculated to be 0.00052 M for a pH of 3.52 (the deposition solution with 25 mM phosphate). The free Cu(II) concentration in the bulk was calculated using the complexation equilibrium listed in Table 1. The actual number should be less than this since the protons are not generated only through the Cu(II) complexation. Thus, the Cu(II) concentration variation should be less than 2.6% (with respect to the total Cu(II) concentration of 0.02 M) and its impact on the diffusion coefficient can be ignored. Based on this understanding, we may assume that the diffusion coefficient of Cu(II) ions in our deposition solutions is a constant. With a diffusion coefficient of 7.2×10^{-6} cm^2 s^{-1}, the thickness of the diffusion layer grows as $\delta(t) = D^{1/2}t^{1/2}$ and *e.g.* at 5 s, it is approximately 60 µm beyond the length of the observed deposits. The steady state current density values indicate a stagnant layer δ of about 200 µm which should then be reached within ~60 s as observed in Fig. 5. The concentration of free Cu(II) ions near the electrode surface in each deposition solution can be calculated using the Cottrell equation. Fig. 6 shows the calculated concentration of free Cu(II) ions at $\delta(5\ \text{s}) = 60$ µm in the presence of different phosphate concentrations. This presents how the free Cu(II) concentration at the electrode surface decreased with the increase of phosphate concentration. Compared to Fig. 3b where the free Cu(II) concentration in the bulk was calculated using the complexation equilibrium listed in Table 1, the free Cu(II) concentrations near the electrode shown in Fig. 6 display the same trend but the actual concentration values are lower.

Growth mechanism of branched-3D-structures in the presence of phosphate

The above results and analyses confirm the competition for free Cu(II) ions between electrodeposition and complexation. Scheme 1 demonstrates the growth of Cu crystals in the absence and presence of phosphate. In the absence of phosphate, the supply of free Cu(II) ions at a low overpotential is sufficient to maintain the uniform deposition of Cu onto the electrode due to the relatively low reduction/deposition rate. Under this condition, the overpotential-limited growth occurs without any Cu(II) depletion zone.[32,37] The shape of the deposited crystals will be dictated by the minimum crystal surface energy and the crystal habit plays a dominant role in determining the shape. When phosphate is introduced into the deposition solution, the Cu(II) concentration decreases due to the complexation with phosphate. At the same relative low overpotential, as free Cu(II) ions near the electrode surface are used up by deposition, a depletion zone forms due to the insufficient Cu(II) supply. Under this condition, the mass transport-limited crystal growth occurs. The growth of Cu depends more on the limited diffusion of free Cu(II) from the bulk solution to the region near the electrode surface. The possibility that the copper phosphate complex adsorbed on the deposited copper surface may further inhibit the free Cu(II) transport. In the depletion layer, the electric field convergence at the corners creates higher current densities of electromigration at protrusions than that at the flat parts, which drives the deposition preferentially at the corners.[37] Finally, branched 3D structures formed even at this relatively low overpotential.

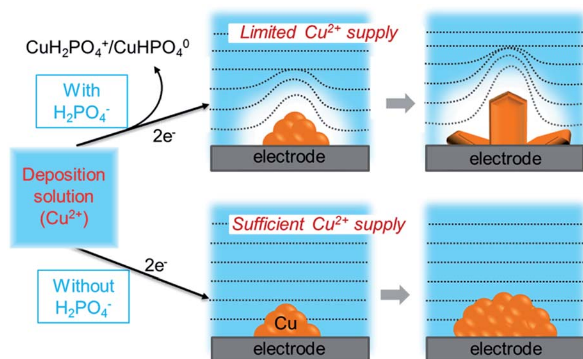

Scheme 1 The mechanism of Cu growth in the absence and the presence of phosphate ions at the same low overpotential.

Electrochemical reduction of CO_2

The as-deposited Cu crystals under various conditions on Cu foil were then investigated for their catalytic performance of CO_2 reduction. The samples made on FTO substrates were not used since SnO_2 in FTO was getting reduced under the experimental conditions (Fig. S6†). The measurements were conducted in CO_2-saturated "wet" acetonitrile (without further drying treatment, 46–528 ppm water content[47]) with 0.1 M tetrabutylammonium tetrafluoroborate as the electrolyte. Fig. S7† shows *I–t* curves recorded during the experiment at −1.45 V *vs.* the NHE (the reference electrode was calibrated using the redox of Fc^+/Fc, the detailed information is provided in the ESI†). The reduction currents were relatively stable for the 1 h (3600 s) duration of the experiment. Fig. 7a shows the faradaic efficiency of the CO_2 reduction products from typical Cu electrodes. The detectable products were HCOOH, CO, and H_2. HPLC and GC were used to quantify these products and the corresponding spectra are given in Fig. S8.† As a control experiment, the polished Cu foil substrate without Cu deposition was tested first. It exhibited a high reduction current density (Fig. S7†), but the major product was CO and its HCOOH selectivity was only ~33%. For the Cu deposited in 10 and 25 mM phosphate at −0.6 V, the faradaic efficiency of HCOOH was up to ~80%, much higher than that by Cu foil. This high selectivity for HCOOH is among the most active electrocatalysts reported recently (the activities of reported Cu-based electrocatalysts for CO_2 reduction are summarized in Table S3†). To find the reasons for this high HCOOH selectivity, the Cu electrodes deposited in 5 mM phosphate at −0.25 V and −0.6 V were investigated. These two electrodes exhibited a similar HCOOH selectivity: *i.e.*, the Cu electrode deposited at −0.25 V gave ~68% HCOOH selectivity and that deposited at −0.6 V gave ~70% HCOOH selectivity. Although many reports have shown that the morphology of electrodes can affect the final products of CO_2 reduction in an aqueous electrolyte (Table S3†),[13,55–60] we didn't find that the morphology plays a significant role here in promoting the formate production. This is probably due to the

View Article Online

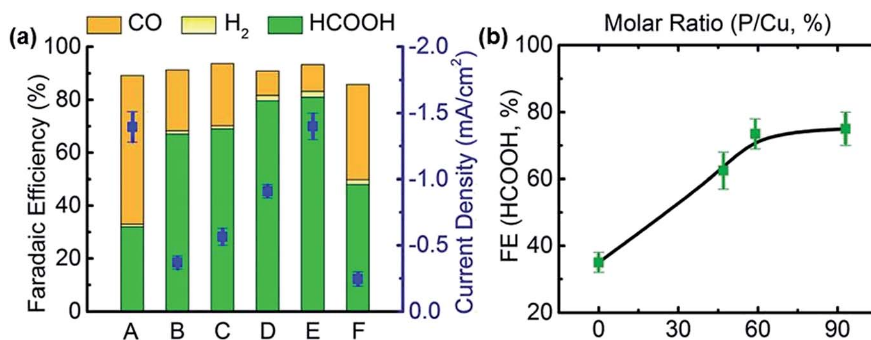

Fig. 7 (a) Faradaic efficiency of the CO_2 reduction products during electrolysis at −1.45 V *vs.* the NHE for 1 h, A–Cu foil, B–Cu deposited in 5 mM phosphate at −0.25 V, C–Cu deposited in 5 mM phosphate at −0.6 V, D–Cu deposited in 10 mM phosphate at −0.6 V, E-Cu deposited in 20 mM phosphate at −0.6 V, F–Cu after stripping phosphate off from sample *D*; current density as calculated from what area – the total Cu area or the capacitance derived one? (b) Faradaic efficiency of HCOOH (average value from a number of measurements) *versus* the P/Cu ratio in the prepared Cu samples (the deposited Cu films were stripped off using scotch tape from the substrate and the P/Cu ratio was obtained by EDS analysis). The standard error is calculated by dividing the standard deviation by the square root of number of measurements. The electrolyte used was CO_2-saturated "wet" acetonitrile (0.1 M tetrabutylammonium tetrafluoroborate).

use of an organic electrolyte system. For example, 90% faradaic efficiency of formate was achieved by using the particle-like Cu composite electrode in the DMF electrolyte, while it is much lower in the aqueous electrolyte.[19] As observed in our control experiments, phosphate ligands indeed play a dominant role in promoting the formate selectivity.

Attention was then paid to a comparison among the three branched-3D-structures deposited at −0.6 V with a similar morphology and surface roughness (the experimental details for double layer capacitance and calculation of the surface roughness are provided in Fig. S9†), but with different phosphate concentrations. In Fig. 7a, it can be seen that the electrodes deposited in 10 and 25 mM phosphate gave higher HCOOH selectivity than that deposited in 5 mM phosphate. It indicates that probably phosphate plays a role in facilitating HCOOH production. In our previous work, we showed that chemisorption of phosphate anions on Cu is strong during electro-reduction and that the phosphate possibly gets attached to the low coordinated sites on Cu as ligands. We inferred that a higher concentration of phosphate could lead to a higher amount of adsorbed phosphate ligands on deposited Cu. The EDS composition analysis also confirmed the presence of phosphorus (Fig. S10†). To quantify the amount of deposited Cu on these three electrodes, the deposited layers were stripped off the Cu foil substrate using conductive carbon tape. The deposition layers on the tape were then examined by SEM-EDS mapping. The EDS analyses show that the P/Cu ratios for the layers deposited in 5, 10, and 25 mM phosphate are 0.47/100, 0.59/100, and 0.93/100, respectively. It is clear that the amount of phosphate ligands on the deposition layer indeed increases if a higher phosphate concentration is employed for deposition. Given that it reaches as high as ∼1% one could roughly expect a 1 nm layer on a Ø 100 nm dendrite, in agreement with the TEM observations that thicker layers were not present. By plotting the faradaic efficiency of HCOOH *versus* the P/Cu ratio, a correlation could be found in Fig. 7b. As shown in the plot, the HCOOH yield increases with the increase of phosphate ligands. It implies that the promoted HCOOH production should be ascribed to the phosphate ligands on the Cu surface. To further confirm it, the prepared Cu electrode was held at a negative potential in 0.1 M Na_2SO_4 for 1 h to strip off phosphate ligands. After stripping, the deposition layer was again analysed by EDS and it was found that the P content dropped to an undetectable level. SEM investigation shows that the morphology of the branched-3D-structure remained unchanged (Fig. 8 and S11†). This electrode was then tested for CO_2 reduction again.

The analysis of the products obtained showed that the HCOOH yield dropped from 79% to 48% (Fig. 8), close to that of the plain Cu foil of 33%. This control experiment suggested that the phosphate ligands play a major role in promoting HCOOH production and the surface morphology may not have a significant impact on it. To further confirm the existence of phosphate ligands on these Cu electrodes, the deposited Cu crystals were scratched off from the substrate and measured for zeta-potential and ATR-FTIR analysis.

Fig. 9 shows the zeta potentials of the samples prepared with and without phosphate. The Cu crystals were dispersed in deionized water to form a 0.5 mg ml^{-1} aqueous suspension and then sonicated for 5 h to achieve a stable suspension in water.

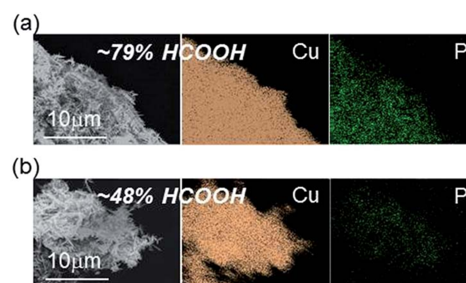

Fig. 8 SEM and the corresponding EDS mapping images of (a) Cu deposited in the presence of 10 mM phosphate at −0.6 V and (b) the same sample after stripping phosphate ligands off in 0.1 M Na_2SO_4 at −1.1 V *vs.* Ag/AgCl for 1 h.

This journal is © The Royal Society of Chemistry 2017

Published on 15 May 2017. Downloaded by University of California - Berkeley on 7/20/2018 5:36:13 PM.

Published on 15 May 2017. Downloaded by University of California - Berkeley on 7/20/2018 5:36:13 PM.

Each sample was tested three times. The zeta potential for bare Cu (deposited at −0.8 V without phosphate) is slightly positive at 0.8 mV, close to deionized water 0 mV. As for the Cu crystals deposited at −0.6 V with 5, 10, and 25 mM phosphate, their zeta potentials are negative at −10.9, −7, and −8.6 mV, respectively. These results are in agreement with other studies, in which it was reported that there is a negative shift of zeta potential after phosphate adsorption (*e.g.* from +10 mV to −15 mV at pH = 7).[61] After stripping the surface phosphate off, the zeta potential shifts back to a positive value at 4.3 mV.

Fig. 10a and b show the ATR-FTIR spectra of the Cu electrode prepared in 10 mM phosphate at −0.6 V after running a CO_2 reduction experiment. Fig. 10e and f are reference curves for the $Cu_3(PO_4)_2\cdot 3H_2O$ precipitate and phosphate liquid solution KH_2PO_4. The composed bands between 1250 cm^{-1} and 903 cm^{-1} are mainly from the P–O symmetric (ν_s) and antisymmetric (ν_{as}) stretching vibration of PO_4 groups,[62–65] indicating the presence of phosphate ligands. In addition, the splitting patterns of four peaks at 1140, 1055, 1010, 903 cm^{-1} in Fig. 10a indicate the formation of both monodentate and bidentate complexes on the Cu surface.[62] After CO_2 reduction, these peaks still existed on the Cu surface (Fig. 10b). Fig. 10c shows the data for Cu crystals after phosphate stripping. No bands of the PO_4 group are apparent in this sample. The regeneration of the phosphate ligands onto the Cu surface after phosphate stripping was tried by the cyclic voltammetry cycling method (Fig. S12a†). During regeneration, the Cu surface went through oxidation and reduction cycles in phosphate buffer solution. After regeneration, stretching vibration of PO_4 groups reappeared (Fig. 10d) as a broad band in the region 1200–900 cm^{-1}. This broad band indicates that the adsorbed phosphate is mainly in the form of monodentate complex.[61,62] After phosphate regeneration, the HCOOH selectivity increased to 65% from 48% of the Cu after phosphate stripping and the surface morphology of the electrode remained unchanged after CO_2 reduction (Fig. S12b†). Possible molecular geometries of monodentate and bidentate complexes are provided in Fig. S13.† In these adsorption states, Cu is connected with phosphate through binding with oxygen. This predominantly occurs with

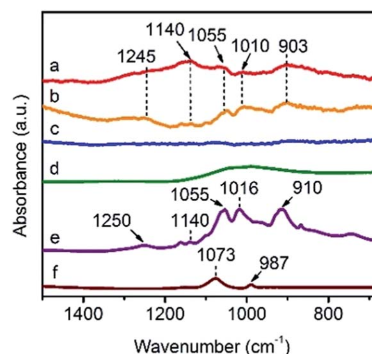

Fig. 10 ATR-FTIR spectra of (a) Cu prepared in 10 mM phosphate at −0.6 V; (b) Cu after CO_2 reduction; (c) Cu after stripping off surface phosphate; (d) Cu after phosphate regeneration; (e) $Cu_3(PO_4)_2\cdot 3H_2O$; (f) liquid phosphate solution (KH_2PO_4).

surface Cu in a low-coordination state. In our previous investigation, we showed that the phosphate ligands are able to improve the proton transport at the surface and thus an enhanced hydrogen production can be observed in aqueous media such as $KHCO_3$ which will lead to the suppression of CO_2 reduction. To minimize the competition from hydrogen generation, the CO_2 reduction was conducted in an organic electrolyte with a limited proton source. Acetonitrile was chosen since it supports a large electrochemical window and has been employed for CO_2 electrolysis, where the solubility of CO_2 with a low water concentration is approximately 300 mM, more than eight times higher than the corresponding amounts of aqueous solution.[66,67]

In the reduction of CO_2 to formic acid, the addition of the first proton to carbon is critical.[68,69] Recently, the insertion of CO_2 into metal-hydride species has been reported as a possible initial step to allow the addition of protons to carbon.[70–74] For example, a metal hydride complex like iridium dihydride complex, may allocate a proton to the carbon of adsorbed CO_2 at the initial step giving rise to high selectivity of formate production (85–95% faradaic efficiency).[70–72] Metal hydride initiated formic acid production has been found on pure metal surfaces as well. For example, CO is the major product on metallic Pd, while formic acid becomes the major product if the Pd surface is electrochemically converted to Pd-hydride (PdH_x).[73] In such a metal-hydride process, it is important to have a proton source for hydride generation, but without generating hydrogen (H_2).[74] In this work, one possible mechanism for promoted formic acid production is the formation of Cu-hydride, which might have resulted from the surface phosphate ligands.

We should note that here the Cu-hydride formation is highly possible because the reduction of H^+ to H is thermodynamically easier than the reduction of CO_2 to $CO_2^{\bullet -}$ at this potential. The phosphate ligands on the Cu surface play a critical role in supplying protons in the following reduction steps. And more protons can be obtained from the "wet" acetonitrile. This can be confirmed by the electrochemical hydrogenation of nitrobenzene Ph-NO_2 to phenyl hydroxyl amine Ph-NHOH and aniline

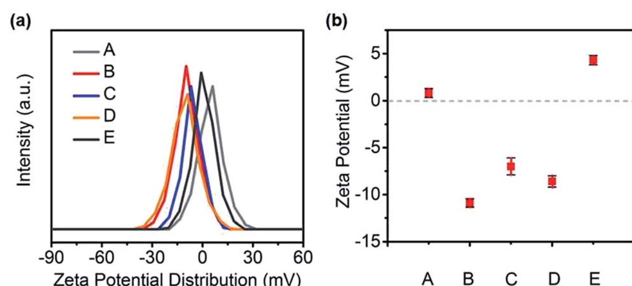

Fig. 9 (a) Zeta potential distribution in deionized (DI) water for the bare Cu crystals prepared in the absence of phosphate at −0.8 V (A), Cu crystals prepared in the presence of phosphate 5 (B), 10 (C), 25 mM (D) phosphate at −0.6 V, and Cu crystals after stripping phosphate off sample c (E). (b) Zeta potential value with the standard error, calculated by dividing the standard deviation by the square root of the number of measurements. All the samples are tested three times.

Published on 15 May 2017. Downloaded by University of California - Berkeley on 7/20/2018 5:36:13 PM.

Ph-NH_2 in the argon-saturated "wet" acetonitrile (Fig. S14†). A possible reaction mechanism for Cu with adsorbed phosphate ligands to reduce CO_2 to HCOOH is shown in Scheme 2. First, the phosphate ligands attached to the surface Cu atoms are able to promote the formation of Cu-hydride [Cu(δ^+)–H(δ^-)] by supplying a proton to Cu as it receives one electron (step 1). This metal hydride species may evolve into hydrogen gas as the major product in aqueous solution due to the easy availability of protons.[38,75,76] However, in a proton lacking system, like an organic electrolyte, the insertion of CO_2 into metal-hydride species will be dominant. The hydride site [H(δ^-)] attacks the carbon atom of CO_2 since it is susceptible to the nucleophilic attack, while the copper site [Cu(δ^+)] attacks one oxygen atom of CO_2 because the oxygen atoms are susceptible to electrophilic attack (step 2).[74,77] This results in the formation of the HCOO⋯Cu inter-mediate.[69,74,77] The phosphate ligand may readily attract a proton from the electrolyte to recover its original state (step 3). In the next step, this original-state phosphate ligand supplies a proton to HCOO⋯Cu as it receives another electron, forming formic acid (HCOOH).[69,73] Finally, the phosphate ligand attracts a proton from the solution and returns to its original state again.

The Tafel slope is as large as 300 mV dec^{-1} (Fig. S15†), similar to Zn dendrites (260 mV dec^{-1}) in aqueous solution and Cu dendrites (300–400 mV dec^{-1}) in ionic liquid for CO_2 electrolysis at high overpotentials.[78,79] The value is not close to commonly observed 60 mV dec^{-1} (a reversible transfer of one electron to CO_2 to form $CO_2^{\bullet-}$ prior to a chemical rate-determining step) or 120 mV dec^{-1} (the first electron transfer to adsorbed CO_2 is the rate determining step) may suggest different mechanisms. The high value of the Tafel slope is probably indicative of current limitation in the organic solvent by mass transport phenomena including both CO_2 diffusion and proton migration. The high value of the Tafel slope is probably an indicative of current limitation in the organic solvent by mass transport phenomena including both CO_2 diffusion and proton migration within the 3D or dendrites structures.

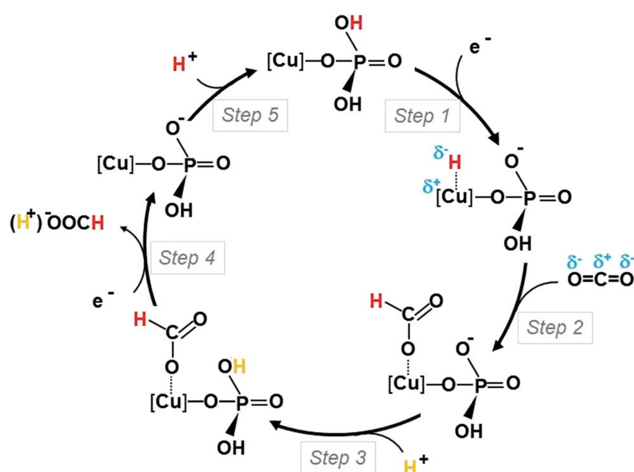

Scheme 2 Possible CO_2 reduction mechanism for HCOOH production on the Cu surface with phosphate ligands.

Recently, a mixture of metallic Cu, copper(I) oxide, and [Cu(cyclam)]$(ClO_4)_2$ complexes was found to be favourable to formic acid production.[19] It exhibited much higher yield for formic acid than the electro-polished polycrystalline Cu plate and electrodeposited Cu. It was suggested that the organic ligand in the complex may participate in proton transfer or capture of CO_2 molecules. We believe, a similar phenomenon is highly possible in our system too. Evidence for the extraordinary ability of phosphate ligands to transfer protons has been observed in many systems.[52,61,80,81] However, there is no report to date about its ability to capture CO_2.

Conclusions

In summary, we have demonstrated that introducing phosphate into the deposition solution leads to the formation of Cu-phosphate complexes. This complexation process competes with the electrodeposition process for free Cu(II) ions. As a result, Cu thin films with branched-3D-structures can be produced at a very small overpotential. The as-prepared Cu electrodes exhibited increased formic acid production. The phosphate ligands on Cu surfaces were believed to be responsible for the enhanced ability to form formic acid. The presence of phosphate ligands probably facilitates the formation of Cu-hydrides, which is a critical initial step for attaching protons onto the carbon atom of adsorbed CO_2 and thus for subsequent formic acid formation. The reported approach is promising to be extended to produce phosphate modified Cu surfaces on various conductive substrates and thus has potential to be employed in CO_2 gas diffusion electrodes for formic acid production.

Acknowledgements

This work is supported by the MOE Tier 1 (RG131/14) and Tier 2 (MOE2015-T2-1-020) Grants of Singapore and by the Singapore National Research Foundation under its Campus for Research Excellence And Technological Enterprise (CREATE) programme as well as Funding from the Danish Research Council for Technology and Production Case No. 12–126194. J. Z. thanks Singapore-Berkeley Research Initiative for Sustainable Energy (SinBeRISE) CREATE for postdoctoral fellowship and financial supports. We thank the Facility for Analysis, Characterisation, Testing and Simulation (FACTS) in Nanyang Technological University for materials characterization.

Notes and references

1 X. Guo, C. Hao, G. Jin, H. Y. Zhu and X. Y. Guo, *Angew. Chem.*, 2014, **53**, 1973–1977.
2 B. C. Ranu, R. Dey, T. Chatterjee and S. Ahammed, *ChemSusChem*, 2012, **5**, 22–44.
3 A. Marimuthu, J. W. Zhang and S. Linic, *Science*, 2013, **339**, 1590–1593.
4 J. Graciani, K. Mudiyanselage, F. Xu, A. E. Baber, J. Evans, S. D. Senanayake, D. J. Stacchiola, P. Liu, J. Hrbek, J. F. Sanz and J. A. Rodriguez, *Science*, 2014, **345**, 546–550.

 This journal is © The Royal Society of Chemistry 2017

Published on 15 May 2017. Downloaded by University of California - Berkeley on 7/20/2018 5:36:13 PM.

5 K. P. Kuhl, E. R. Cave, D. N. Abram and T. F. Jaramillo, *Energy Environ. Sci.*, 2012, **5**, 7050–7059.

6 K. J. Schouten, Y. Kwon, C. J. van der Ham, Z. Qin and M. T. M. Koper, *Chem. Sci.*, 2011, **2**, 1902–1909.

7 Y. W. Lum, Y. K. Kwon, P. Lobaccaro, L. Chen, E. L. Clark, A. T. Bell and J. W. Ager, *ACS Catal.*, 2016, **6**, 202–209.

8 Y. K. Kwon, Y. W. Lum, E. L. Clark, J. W. Ager and A. T. Bell, *ChemElectroChem*, 2016, **3**, 1012–1019.

9 Y. Hori, A. Murata and R. J. Takahashi, *J. Chem. Soc., Faraday Trans. 1*, 1989, **85**, 2309–2326.

10 R. Kas, K. K. Hummadi, R. Kortlever, P. Wit, A. Milbrat, M. W. Luiten-Olieman, N. E. Benes, M. T. M. Koper and G. Mul, *Nat. Commun.*, 2016, **7**, 10748.

11 C. W. Li and M. W. Kanan, *J. Am. Chem. Soc.*, 2012, **34**, 7231–7234.

12 D. Ren, Y. Deng, A. D. Handoko, C. S. Chen, S. Malkhandi and B. S. Yeo, *ACS Catal.*, 2015, **5**, 2814–2821.

13 R. Reske, H. Mistry, F. Behafarid, B. R. Cuenya and P. Strasser, *J. Am. Chem. Soc.*, 2014, **136**, 6978–6986.

14 Z. Xu, E. Lai, Y. Shao-Horn and K. Hamad-Schifferli, *Chem. Commun.*, 2012, **48**, 5626–5628.

15 K. P. Rice, E. J. Walker, M. P. Stoykovich and A. E. Saunders, *J. Phys. Chem. C*, 2011, **115**, 1793–1799.

16 W. Tang, A. A. Peterson, A. S. Varela, Z. P. Jovanov, L. Bech, W. J. Durand, S. Dahl, J. K. Norskov and I. Chorkendorff, *Phys. Chem. Chem. Phys.*, 2012, **14**, 76–81.

17 J. Qiao, P. Jiang, J. Liu and J. Zhang, *Electrochem. Commun.*, 2014, **38**, 8–11.

18 M. S. Xie, B. Y. Xia, Y. W. Li, Y. Yan, Y. H. Yang, Q. Sun, S. H. Chan, A. Fisher and X. Wang, *Energy Environ. Sci.*, 2016, **9**, 1687–1695.

19 T. N. Huan, E. S. Andreiadis, J. Heidkamp, P. Simon, E. Derat, S. Cobo, G. Royal, A. Bergmann, P. Strasser, H. Dau, V. Artero and M. Fontecave, *J. Mater. Chem. A*, 2015, **3**, 3901–3907.

20 S. Rasul, D. H. Anjum, A. Jedidi, Y. Minenkov, L. Cavallo and K. Takanabe, *Angew. Chem.*, 2015, **54**, 2146–2150.

21 M. V. Mandke and H. M. Pathan, *J. Electroanal. Chem.*, 2012, **686**, 19–24.

22 C. J. Yang and F. H. Lu, *Langmuir*, 2013, **29**, 16025–16033.

23 R. Qiu, X. L. Zhang, R. Qiao, Y. Li, Y. I. Kim and Y. S. Kang, *Chem. Mater.*, 2007, **19**, 4174–4180.

24 S. Wu, Z. Yin, Q. He, G. Lu, Q. Yan and H. Zhang, *J. Phys. Chem. C*, 2011, **115**, 15973–15979.

25 Y. J. Han, X. Zhang and G. W. Leach, *Langmuir*, 2014, **30**, 3589–3598.

26 J. Y. Sun, H. R. Lee and K. H. Oh, *Sci. Rep.*, 2015, **5**, 13791.

27 X. Wu, F. Chen, Y. Jin, N. Zhang and R. L. Johnston, *ACS Appl. Mater. Interfaces*, 2015, **7**, 17782–17791.

28 J. Y. Zheng, Z. L. Quan, G. Song, C. W. Kim, H. G. Cha, T. W. Kim, W. Shin, K. J. Lee, M. H. Jung and Y. S. Kang, *J. Mater. Chem.*, 2012, **22**, 12296–12304.

29 M. J. Siegfried and K. S. Choi, *Angew. Chem.*, 2005, **44**, 3218–3223.

30 M. J. Siegfried and K. S. Choi, *Angew. Chem.*, 2008, **47**, 368–372.

31 C. M. López and K. S. Choi, *Langmuir*, 2006, **22**, 10625–10629.

32 K. S. Choi, *Dalton Trans.*, 2008, **40**, 5432–55438.

33 R. Venkatasubramanian, J. He, M. W. Johnson, I. Stern, D. H. Kim and N. S. Pesika, *Langmuir*, 2013, **29**, 13135–13139.

34 M. D. Susman, Y. Feldman, A. Vaskevich and I. Rubinstein, *ACS Nano*, 2014, **8**, 162–174.

35 Z. L. Xiao, C. Y. Han, W. K. Kwok, H. H. Wang, U. Welp, J. Wang and G. W. Crabtree, *J. Am. Chem. Soc.*, 2004, **126**, 2316–2317.

36 A. Osherov, C. Zhu and M. Panzer, *Chem. Mater.*, 2013, **25**, 692–698.

37 C. P. Nielsen and H. Bruus, *Phys. Rev. E: Stat., Nonlinear, Soft Matter Phys.*, 2015, **92**, 042302.

38 J. Zhao, P. D. Tran, Y. Chen, J. S. C. Loo, J. Barber and Z. C. J. Xu, *ACS Catal.*, 2015, **5**, 4115–4120.

39 M. Edwards, L. Hidmi and D. Gladwel, *Corros. Sci.*, 2002, **44**, 1057–1071.

40 D. E. Macnevin, PhD thesis, University of Central Florida, 2007.

41 E. D. Stone, PhD thesis, University of Central Florida, 2008.

42 L. Guo, S. Zhang, B. Ju and J. Yang, *Carbohydr. Polym.*, 2006, **63**, 487–492.

43 Y. Moreno, A. Vega, S. Ushak, R. Baggio, O. Pena, E. Le Fur, J. Y. Pivan and E. Spodine, *J. Mater. Chem.*, 2003, **13**, 2381–2387.

44 W. Mohl, A. Schweiger and H. Motschi, *Inorg. Chem.*, 1990, **29**, 1536–1543.

45 S. H. Reiber, *J.–Am. Water Works Assoc.*, 1989, **81**, 114–122.

46 S. Geose, *Acta Crystallogr.*, 1963, **16**, 124–128.

47 M. C. Figueiredo, I. L. Yanez and M. T. M. Koper, *ACS Catal.*, 2016, **6**, 2382–2392.

48 K. Fukami, S. Nakanishi, H. Yamasaki, T. Tada, K. Sonoda, N. Kamikawa, N. Tsuji, H. Sakaguchi and Y. Nakato, *J. Phys. Chem. C*, 2007, **111**, 1150–1160.

49 T. C. Liu, C. M. Liu, H. Y. Hsiao, J. L. Lu, Y. S. Huang and C. Chen, *Cryst. Growth Des.*, 2012, **12**, 5012–5016.

50 J. Chung, D. H. Won, J. Koh, E. H. Kim and S. I. Woo, *Phys. Chem. Chem. Phys.*, 2016, **18**, 6252–6258.

51 S. Aksu, *J. Electrochem. Soc.*, 2009, **156**, C387–C394.

52 M. K. Coggins, M. T. Zhang, Z. Chen, N. Song and T. J. Meyer, *Angew. Chem.*, 2014, **53**, 12226–12230.

53 J. T. Hinatsu and F. R. Foulkes, *J. Electrochem. Soc.*, 1989, **136**, 125–132.

54 T. I. Quickenden and Q. Xu, *J. Electrochem. Soc.*, 1996, **143**, 1248–1253.

55 H. Mistry, A. S. Varela, S. Kühl, P. Strasser and B. R. Cuenya, *Nat. Rev. Mater.*, 2016, **1**, 16009.

56 F. S. Roberts, K. P. Kuhl and A. Nilsson, *Angew. Chem., Int. Ed.*, 2015, **54**, 5179–5182.

57 A. Loiudice, P. Lobaccaro, E. A. Kamali, T. Thao, B. H. Huang, J. W. Ager and R. Buonsanti, *Angew. Chem., Int. Ed.*, 2016, **55**, 5789–5792.

58 M. Ma, K. Djanashvili and W. A. Smith, *Angew. Chem., Int. Ed.*, 2016, **55**, 6680–6684.

59 K. D. Yang, W. R. Ko, J. H. Lee, S. J. Kim, H. Lee, M. H. Lee and K. T. Nam, *Angew. Chem., Int. Ed.*, 2017, **56**, 796–800.

Published on 15 May 2017. Downloaded by University of California - Berkeley on 7/20/2018 5:36:13 PM.

60 S. Sen, D. Liu and G. T. R. Palmore, *ACS Catal.*, 2014, **4**, 3091–3095.

61 J. Y. Kim, J. W. Jang, D. H. Youn, G. Magesh and G. S. Lee, *Adv. Energy Mater.*, 2014, **4**, 1400476.

62 G. Rubasinghege, P. K. Kyei, M. M. Scherer and V. H. Grassian, *J. Colloid Interface Sci.*, 2012, **385**, 15–23.

63 L. Körösi, S. Papp, I. Bertóti and I. Dékány, *Chem. Mater.*, 2007, **19**, 4811–4819.

64 E. Elzinga and D. L. Sparks, *J. Colloid Interface Sci.*, 2007, **308**, 53–70.

65 W. Q. Gong, *Int. J. Miner. Process.*, 2001, **63**, 147–165.

66 Y. Tomita, S. Teruya, O. Koga and Y. Hori, *J. Electrochem. Soc.*, 2000, **174**, 4164–4167.

67 M. R. Jonnathan, L. D. John and R. Joel, *J. Am. Chem. Soc.*, 2014, **136**, 8361–8367.

68 M. J. Cheng, Y. Kwon, M. Head-Gordon and A. T. Bell, *J. Phys. Chem. C*, 2015, **119**, 21345–21352.

69 R. Kortlever, J. Shen, K. J. Schouten, F. Calle-Vallejo and M. T. M. Koper, *J. Phys. Chem. Lett.*, 2015, **6**, 4073–4082.

70 P. Kang, C. Cheng, Z. Chen, C. K. Schauer, T. J. Meyer and M. Brookhart, *J. Am. Chem. Soc.*, 2012, **134**, 5500–5503.

71 P. Kang, S. Zhang, T. J. Meyer and M. Brookhart, *Angew. Chem.*, 2014, **53**, 8709–8713.

72 P. Kang, T. J. Meyer and M. Brookhart, *Chem. Sci.*, 2013, **4**, 3497–3502.

73 X. Min and M. W. Kanan, *J. Am. Chem. Soc.*, 2015, **137**, 4701–4708.

74 P. Kang, Z. Chen, M. Brookhart and T. J. Meyer, *Top. Catal.*, 2014, **58**, 30–45.

75 R. M. Bullock, A. M. Appel and M. L. Helm, *Chem. Commun.*, 2014, **50**, 3125–3143.

76 B. Choi, D. Panthi, M. Nakoji, T. Kabutomori, K. Tsutsumi and A. Tsutsumi, *Int. J. Hydrogen Energy*, 2015, **40**, 6197–6206.

77 E. E. Benson, C. P. Kubiak, A. J. Sathrum and J. M. Smieja, *Chem. Soc. Rev.*, 2009, **38**, 89–99.

78 J. Rosen, G. S. Hutchings, Q. Lu, R. V. Forest, A. Moore and F. Jiao, *ACS Catal.*, 2015, **5**, 4586–4591.

79 T. N. Huan, P. Simon, G. Rousse, I. Génois, V. Artero and M. Fontecave, *Chem. Sci.*, 2017, **8**, 742–747.

80 M. W. Kanan, Y. Surendranath and D. G. Nocera, *Chem. Soc. Rev.*, 2009, **38**, 109–114.

81 S. Cobo, J. Heidkamp, P. A. Jacques, J. Fize, V. Fourmond, L. Guetaz, B. Jousselme, V. Ivanova, H. Dau, S. Palacin, M. Fontecave and V. Artero, *Nat. Mater.*, 2012, **11**, 802–807.

This journal is © The Royal Society of Chemistry 2017